Deducing primary γ-ray intensities and the dipole strength function in ^{94}Mo via radiative proton capture

F. Heim,[1,*] J. Mayer,[1] M. Müller,[1] P. Scholz,[1,2] and A. Zilges[1]
[1]*University of Cologne, Institute for Nuclear Physics, 50937 Köln, Germany*
[2]*Department of Physics, University of Notre Dame, Notre Dame, Indiana 46556-5670, USA*

(Received 5 November 2020; accepted 8 February 2021; published 18 February 2021)

Background: The nucleosynthesis of heavy nuclei is affected by the reaction rates of radiative capture reactions. Many of the astrophysical relevant rates cannot be obtained from experiments but are obtained from theoretical models. The γ-decay widths that are derived from radiative strength functions are one of the key nuclear physics input parameters in those calculations. The explicit study of γ-ray strength functions has been thoroughly addressed in the last decade and various methods have been established to extract the dipole strength in atomic nuclei.
Purpose: The investigation of primary γ-ray transitions from the ^{93}Nb$(p,\gamma)^{94}$Mo reaction allows deducing the γ-ray strength function in ^{94}Mo. The results are compared to results obtained using other techniques and the impact of level densities, excitation mechanism, and excitation energy will be thoroughly investigated.
Method: The proton beam was delivered by the 10 MV FN-Tandem accelerator located at the Institute for Nuclear Physics at the University of Cologne, Germany. By means of in-beam γ-ray spectroscopy the intensity of primary γ rays is determined. Additionally, the first generation γ-ray intensity is deduced from the secondary γ rays using their branching and the coincidence detection efficiency. Absolute γ-ray strength function values as well as relative values using the ratio method will be extracted.
Results: Numerous states in ^{94}Mo at excitation energies above 3 MeV have been identified for the first time and their decay behavior has been studied. We disentangled the effects of $M1$ and $E1$ radiation for the γ-ray emission channel in ^{94}Mo and extracted strength function curves for both radiation types. Our results are in good agreement with experimental results using the Oslo method and photoinduced experiments as well as with recent theoretical quasiparticle random-phase approximation (QRPA) calculations. An enhancement of the γ-ray strength below the neutron separation energy was found that is most likely of $E1$ character. In addition, a significant increase of the dipole strength at low γ-ray energies was found which is most likely due to $M1$ strength.
Conclusion: Radiative proton capture reactions are a well-suited tool to study the γ-ray strength function in atomic nuclei. From the intensity of primary γ-ray transitions as well as from secondary γ-rays, information about the radiative dipole strength can be extracted. The γ-ray emission seems to be independent of the excitation energy in the studied mass and energy range. Detailed knowledge about the intrinsic properties of the nuclear states is very important and their uncertainties affect the uncertainty of the extracted γ-ray strength functions heavily.

DOI: 10.1103/PhysRevC.103.025805

I. INTRODUCTION

The general photoresponse and γ-ray emission behavior of atomic nuclei is described by the γ-ray strength function (γ-SF). It plays an important role in all kinds of nuclear reaction networks. In particular, the (n,γ) and (γ,n) reaction rates in the *slow* and *rapid* neutron capture processes are heavily affected by the γ-SF [1–4]. Moreover, the γ-ray strength function just above the particle separation threshold is of direct relevance for the p process nucleosynthesis as it affects the photodisintegration rates which transform s- or r-seed nuclei to the neutron deficient side of the nuclear chart [5–7].

γ-ray strength functions have been investigated for several decades. At present, there is no experimental method that provides a full picture of the γ-SFs over a wide energy range. In addition, measuring isolated γ-SFs is challenging, since usually, only a convolution between nuclear level density and γ-SF is experimentally observed. Also, it has been shown that the γ-ray strength function obtained from photoabsorption experiments can depend on the deexcitation strength function [8,9]. Large experimental campaigns revealed several structures caused by different, partly collective phenomena within the atomic nucleus in the past years: At low energies an unexpected enhancement ("up-bend") was found in several medium-mass nuclei. The origin of this enhancement and in particular its radiation type are subjects of current research [10–14]. At energies around the neutron separation

*fheim@ikp.uni-koeln.de

energy, an $E1$ pygmy dipole resonance was found in several nuclei [15]. Both phenomena can affect the reaction rates relevant for nuclear astrophysics significantly [16,17]. For details on the origin of the γ-SF, various methods, experimental results, and available databases for the γ-SF we refer to Ref. [18].

The presumed astrophysical scenario that is responsible for p process nucleosynthesis is a type II supernova (SNII) explosion. However, among others, the light p nuclei ^{92,94}Mo are notoriously underproduced in quantitative calculations of p process yields [19–21]. At present, the nucleosynthesis of light Mo p isotopes remains an unsolved puzzle [5,6,22]. To reduce the uncertainties related to nuclear physics in these networks, detailed knowledge of nuclear statistical properties such as γ-SF and nuclear level density (NLD) is required.

Previously, the γ-ray strength function in ^{94}Mo has been studied by means of different experimental approaches using various probes. Above the neutron separation energy the γ-SF is almost completely described by the photoneutron cross section [23,24]. At lower energies data from (γ,γ') experiments are available [25]. Oslo type experiments provided γ-SF data at γ-ray energies from 1 to 7.4 MeV and were derived from a (^{3}He, ^{3}He) experiment [14]. In this paper we present γ-SF data for $E1$ and $M1$ radiation in ^{94}Mo derived from the primary γ-ray intensities after proton capture on ^{93}Nb. Moreover, we applied the ratio method [26,27] to deduce model-independent, relative strength functions from $\gamma\gamma$ coincidences.

This paper is structured as follows: In Sec. II a brief summary of the experiment is given. In Sec. III two methods to determine the intensity of primary γ-rays as well as their relation to the γ-ray strength function are explained. In Sec. IV the experimental results are presented, followed by a discussion of the derived γ-ray strength function in Sec. V.

II. EXPERIMENTAL DETAILS

The ^{93}Nb$(p,\gamma)^{94}$Mo experiment was performed at the 10 MV FN-Tandem accelerator of the Institute for Nuclear Physics at the University of Cologne. The combination of the Nuclear Astrophysics target chamber and the high-resolution γ-ray spectrometer HORUS was used for the determination of the primary γ-ray intensities. Details on this setup were reported in Ref. [28]. The ^{93}Nb$(p,\gamma)^{94}$Mo reaction was studied by means of in-beam γ-ray spectroscopy. After the bombardment of the ^{93}Nb target nuclei with protons of energy E_p, a highly excited compound nucleus is formed with an excitation energy of $E_x = Q + E_{\mathrm{c.m.}}$. The Q value of the ^{93}Nb$(p,\gamma)^{94}$Mo reaction is 8490 keV. A monoisotopic, metallic ^{93}Nb target of 1.1(1) mg/cm^2 thickness was irradiated at average proton beam intensities of 690 nA for 87 hours and 540 nA for 133 hours at proton energies of $E_p = 3.0$ MeV and $E_p = 3.5$ MeV, respectively.

The target thickness was determined via Rutherford backscattering spectrometry (RBS) at the RUBION facility in Bochum, Germany before and after the experiment. In addition, the target thickness was monitored during the experiment using the RBS detector mounted at the target chamber in Cologne [28]. The proton beam was stopped in a 200 mg/cm^2 thick gold backing to avoid beam-induced background caused by the widened beam behind the target. The energy loss inside the target is calculated using SRIM [29], resulting in total energy losses ΔE of 56 and 62 keV for 3.0 and 3.5 MeV beam energy, respectively. The effective interaction energy of the protons is defined as

$$E_{\mathrm{eff}} = E_p - \frac{\Delta E}{2}, \tag{1}$$

where E_p denotes the beam energy of the impinging protons.

III. DEDUCING PRIMARY γ-RAY INTENSITIES

Primary γ rays (i.e., the *first generation* γ-rays emitted by the reaction product) provide valuable information about the γ-SF in the compound nucleus since it predominantly affects their intensities. Under the assumption that the electromagnetic deexcitation is dominated by dipole transitions, the γ-SF is defined as [30]

$$f_{i\to L}(E_\gamma) = \frac{\langle\Gamma_{i\to L}\rangle_{J^\pi}}{E_\gamma^3}\rho_{J^\pi}(E_i). \tag{2}$$

The strength $f_{i\to L}(E_\gamma)$ of a primary γ-ray transition from a state i at energy E_i to a discrete level L depends on the average partial decay width $\langle\Gamma_{i\to L}\rangle_{J^\pi}$, the level density ρ_{J^π} at E_i, and the γ-ray energy E_γ.

The absolute intensity of a primary γ ray that populates a specific state in the reaction product normalized to the number of projectiles and target thickness is here called *partial cross section*. The total (p,γ) cross-section results of the ^{93}Nb$(p,\gamma)^{94}$Mo reaction that were extracted from this experiment have already been published in Ref. [31]. In this paper we present the studies of the prompt γ-ray deexcitation and two methods to determine the intensity of the *first generation* γ rays.

A. First generation γ rays from singles spectra

The most straightforward way to determine the *first generation* γ-ray intensities is to study the singles γ-ray spectra [32]. The peaks are expected at γ-ray energies of

$$E_\gamma = E_{\mathrm{c.m.}} + Q - E_x, \tag{3}$$

where $E_{\mathrm{c.m.}}$ is the center-of-mass energy of the reaction, Q the Q value of the reaction, and E_x the excitation energy of the populated state. Proton beam energies of 3.0 and 3.5 MeV were chosen. This leads to compound nucleus excitation energies of 11 490 and 11 990 keV, respectively.

The absolute partial cross sections

$$\sigma_{\mathrm{partial}} = \frac{N_{\gamma,i}}{N_P N_T} \tag{4}$$

are determined from the intensity of the primary γ-ray transitions $N_{\gamma,i}$ derived from the singles γ-ray spectra as well as the number of projectiles N_P and target nuclei N_T. This method is described in detail, e.g., in Refs. [28,33,34]. Each emitted γ ray follows an angular distribution $W(\Theta)$ with respect to the beam axis. The experimental yield $Y(E_\gamma)$ is corrected for the full-energy peak efficiency $\epsilon(E_\gamma)$ and the dead time correction

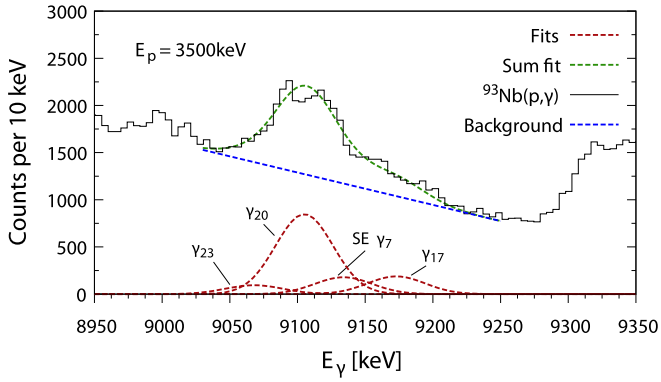

FIG. 1. Region of the singles γ-ray spectrum where primary γ-ray transitions into levels 17, 20, and 23 are expected. In addition, the single-escape peak of γ_7 is expected in this region. The peaks are rather broad due to the energy loss of the protons and an unambiguous identification is difficult. The fits of the different transitions shown in the lower part were performed by fixing the peak positions and widths.

of the data acquisition τ:

$$W(\Theta) = \frac{Y(E_\gamma)}{\epsilon(E_\gamma)\tau}. \tag{5}$$

The angular distribution is obtained by fitting a series of Legendre polynomials to the experimental values:

$$W(\Theta) = A_0\left(1 + \sum_{k=2,4} \alpha_k P_k(\cos\Theta)\right). \tag{6}$$

Finally, the sum of all A_0 coefficients represents the total number of reactions, $N_{(p,\gamma)}$ [28].

According to Eq. (2) the partial cross sections depend not only on the γ-ray strength function but also on the level density in the compound nucleus which needs to be fixed. This issue is thoroughly analyzed in Sec. V A.

B. Second generation γ rays

A recent approach to gather information about the *first generation* γ-ray intensities was utilized in this experiment as well. In general, many prompt γ rays have rather high energies of around 10 MeV and are broadened due to the energy loss of the protons. Consequently, the respective peaks are often difficult to identify. In addition, especially prompt γ rays to states above ≈2 MeV will most likely overlap and cannot be identified unambiguously (see Fig. 1). This issue can be overcome by looking for the *second generation* γ rays. These γ rays depopulate an intermediate state L, that is reached by primary γ-ray transitions, into a final state f (see Fig. 2). Due to the high granularity obtained by using 14 high-purity germanium (HPGe) detectors for γ detection and an event-by-event data format asymmetric $\gamma\gamma$ matrices can be constructed which store all coincidence signals between any pair of detectors. Subsequently, gating on the *second generation* γ ray will uncover the primary γ-ray peak. Its absolute intensity can be derived from the branching $b_{L\to f}$ and

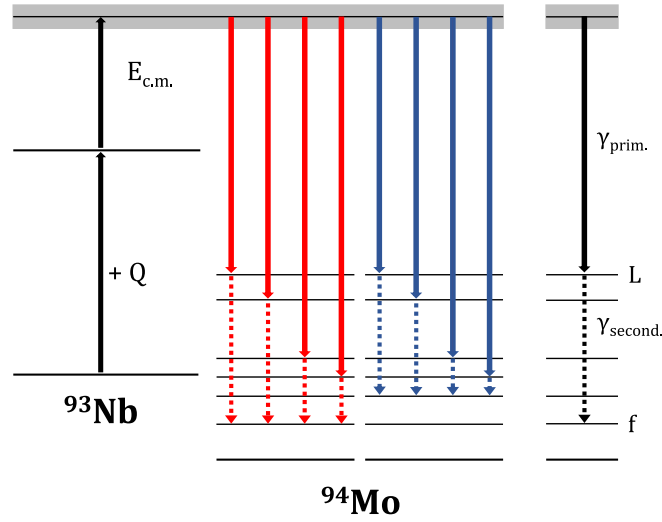

FIG. 2. Illustration of the discrete two-step cascade method. Each solid arrow depicts a primary γ ray that populates a discrete state. Each dashed arrow depicts a *second generation* γ ray. Exemplarily, on the right side (in black) the primary γ-ray transition into a state L is shown. Subsequently, this state deexcites into the final state f via the secondary γ-ray transition. The intensity of primary γ rays can then be determined from the intensity of the secondary transitions. If the intermediate state L can deexcite into different final states the respective branching ratios have to be known and taken into account. For better readability, this is not shown in the figure.

the coincidence efficiency ϵ_{coin}:

$$I_{\gamma,L} = \frac{N_{L\to f}}{\epsilon_{\text{coin}} \times b_{L\to f}} \quad \text{with} \quad \epsilon_{\text{coin}} \propto \sum_{i,j\neq i}^{N_d} \epsilon_i \epsilon_j, \tag{7}$$

where N_d is the number of detectors and ϵ_x the full energy peak efficiency of the respective detector. $N_{L\to f}$ is the number of *second generation* γ rays.

This technique can be refined by setting a condition on the sum of the two γ rays:

$$E_{\gamma,\text{sum}} = E_{\gamma,1} + E_{\gamma,2}, \tag{8}$$

where $E_{\gamma,1}$ ($E_{\gamma,2}$) is a first (second) generation γ ray. Hence, sum peak spectra can be constructed that contain γ-ray events at γ-ray energies $E_{\gamma,\text{sum}}$ which consist of two single γ rays. By construction, these *discrete two-step cascade spectra* show sum peaks at γ-ray energies

$$E_{\gamma,\text{sum}} = E_{\text{c.m.}} + Q - E_x, \tag{9}$$

where E_x denotes the level energy of state $x = 0, 1, 2, \ldots$.

This technique is an ideal tool to apply the ratio method [26] which reduces the uncertainties related to the level density. According to the derivation in Ref. [35] the ratios of primary γ-ray intensities to various final states with identical spins and parities are given by

$$\frac{I_{L_1}}{I_{L_2}} = \frac{f_{E1}(E_{\gamma_1}) + \frac{b}{a} \times f_{M1}(E_{\gamma_1})}{f_{E1}(E_{\gamma_2}) + \frac{b}{a} \times f_{M1}(E_{\gamma_2})} \times \frac{E_{\gamma_1}^3}{E_{\gamma_2}^3}, \tag{10}$$

where I_{L_x} denotes the respective intensity of a γ-ray transition with energy E_{γ_x} and the ratio b/a accounts for the impact of

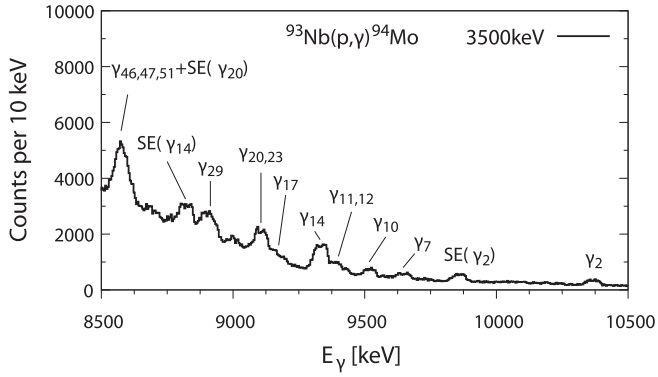

FIG. 3. High energy part of the in-beam singles γ-ray spectrum for an incident proton beam energy of $E_p = 3500$ keV. The positions of primary γ rays which directly populate certain states in ^{94}Mo are marked.

the $M1$ strength. This method has been successfully applied in radiative proton capture reactions on ^{63,65}Cu [35].

IV. EXPERIMENTAL RESULTS

A. Singles γ-ray spectra

The experimental yields from the γ-ray spectra need to be corrected for the full-energy peak efficiencies of the detectors. Therefore, a ^{226}Ra standard calibration source was used for the low-energy efficiency calibration. For relative γ-ray detection efficiencies of γ-ray energies up to 5 MeV, in-house produced ^{56}Co and ^{66}Ga sources were used and were scaled to the absolute efficiencies from the ^{226}Ra source. ^{56}Co and ^{66}Ga have relatively short half-lives of 77 days and 9.5 hours, respectively, but emit numerous γ rays up to an energy of $E_\gamma = 4.8$ MeV [36,37]. The total detection efficiency of the HORUS detector array amounts to about 3% at $E_\gamma = 1.3$ MeV in the configuration used for this experiment. To extrapolate the absolute efficiencies to higher γ-ray energies, the GEANT4 [38,39] toolkit was used as well as a double-exponential fit function. See Ref. [28] for more details.

The ^{93}Nb target nucleus possesses ground-state spin $J_0^\pi = 9/2^+$. After proton capture, predominantly 4^+, 5^+, 4^-, and 5^- states are populated in the compound nucleus which will most likely deexcite via dipole transitions into low-lying states. Figure 3 shows the high-energy part of the singles γ-ray spectrum for incident protons with $E_p = 3.5$ MeV. As expected, prompt γ-ray peaks for transitions into intermediate levels L with $3 \leqslant J_L \leqslant 6$ are observed. Using the singles spectra, 12 partial cross sections for each proton beam energy of 3.0 and 3.5 MeV were determined by means of Eq. (4). The experimentally obtained cross sections can be found in Table I. Note that the experimental width of the prompt γ-ray peaks is consistent with the energy loss within the target obtained from the SRIM simulations.

The spectroscopic information for levels above ≈2.5 MeV is quite scarce and spin-parity assignments are often not unambiguous. The experimental partial cross sections reported in this work go down to ≈100 nb. Note that the experimental cross sections for levels 14, 20, 29, 46/47, and 51 are significantly higher than for other levels. As will be discussed later, this can be explained by the spin and parity of these levels.

TABLE I. Partial cross-section values σ_p for the ^{93}Nb$(p,\gamma)^{94}$Mo reaction for the proton energies of 3.0 and 3.5 MeV. For each partial cross section the spin and parity of the respective level are given. Note that the levels 46 and 47 are very close to each other and contributions from both levels have likely been observed. All level information is taken from Ref. [40].

Level	E_X (keV)	J^π	E_p (MeV)	E_γ (keV)	σ_p (nb)
2	1574	4^+	3.0	9872	306 ± 47
			3.5	10367	705 ± 86
7	2295	4^+	3.0	9151	250 ± 39
			3.5	9646	481 ± 59
10	2423	6^+	3.0	9023	486 ± 60
			3.5	9517	616 ± 75
11	2534	3^-	3.0	8912	270 ± 20
			3.5	9407	611 ± 75
12	2565	4^+	3.0	8881	139 ± 41
			3.5	9376	388 ± 47
14	2611	$(5)^-$	3.0	8836	1133 ± 173
			3.5	9331	2256 ± 276
17	2768	4^+	3.0	8678	128 ± 16
			3.5	9173	436 ± 53
20	2835	$(4)^-$	3.0	8611	676 ± 83
			3.5	9106	1977 ± 242
23	2872	6^+	3.0	8574	326 ± 40
			3.5	9068	254 ± 31
29	3027	(3)	3.0	8419	597 ± 73
			3.5	8914	1447 ± 177
46,47	3367	?	3.0	8080	1099 ± 161
			3.5	8574	2230 ± 273
51	3389	5^-	3.0	8057	436 ± 53
			3.5	8552	946 ± 116

B. Identification of new levels

For an unambiguous identification of the peaks visible in the γ-ray spectra, precise knowledge about the nuclear level scheme of ^{94}Mo is required. In particular, reliable γ-decay branching ratios from certain levels need to be known to apply the two-step cascade (TSC) ratio method as explained in Sec. III B. For this purpose, the particle-γ coincidence technique was applied. The coincident measurement of scattered particles on a target nucleus of interest and the emitted γ-rays enables one to construct a particle-γ matrix (see Fig. 4). This matrix contains all events where one particle detector and at least one γ-ray detector measured an energy deposition. The columns visible in the matrix correspond to a certain excitation energy E_X. By requiring this energy as a gate (allowing a certain width ΔE_X) and projecting the resulting spectrum on the γ-ray energy axis will reveal the complete γ-ray decay pattern of levels within this excitation energy region. In addition, decays directly back into the ground state are visible in the ground-state diagonal for which the excitation energy E_X matches the γ-ray energy E_γ. Similarly, decays into certain final levels with energy E_f generate additional diagonals for which the condition $E_\gamma + E_f \approx E_X$ holds. Gating on these

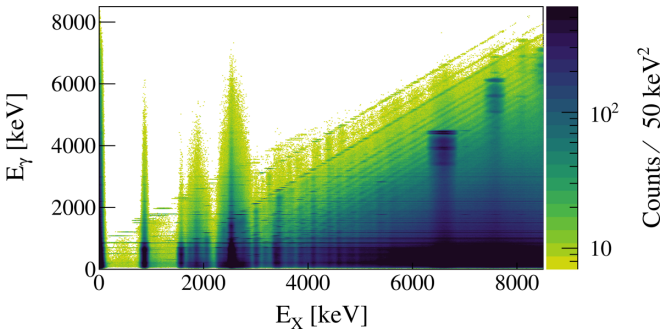

FIG. 4. Proton-γ coincidence matrix for the ^{94}Mo$(p, p')^{94}$Mo reaction at $E_p = 13.5$ MeV. E_X is the excitation energy of the nucleus, calculated from the ejectile energy. E_γ is the measured γ-ray energy. For details, see Ref. [41].

diagonals, again, provides clean γ-ray spectra which only contain transitions to the ground state (or some other excited state).

A ^{94}Mo$(p, p')^{94}$Mo experiment using the combined particle-γ spectrometer SONIC@HORUS was performed at the University of Cologne, from which the p-γ-matrix shown in Fig. 4 was extracted. The particle-γ coincidence technique and the SONIC@HORUS spectrometer are described in detail in Ref. [41]. By means of the proton-γ matrix, 39 formerly unknown levels in ^{94}Mo were identified as well as numerous new transitions. In the Appendix, we provide a full table of all low-lying levels in ^{94}Mo which show at least two γ-decays to lower lying levels as well as all newly identified levels. In particular, levels above $\approx$3 MeV that decay into the ground and/or first excited state could be identified via the diagonal gates unambiguously. Moreover, relative γ-ray intensities $I_\gamma(i) = I_f(i)/I_j(i)$ were determined for transitions from level i to level f, normalized to the strongest decay to level j. The new spectroscopic level information was used in the analysis of the ^{93}Nb$(p, \gamma)^{94}$Mo reaction, which will be discussed in the following sections.

C. Discrete two-step cascade spectra

The yield of primary γ-rays was additionally obtained from discrete TSC spectra [42,43]. Although this method was originally developed to study models for the γ-ray strength function and nuclear level density in (n, γ) reactions, it was recently applied in (p, γ) reactions [35]. Due to the energy loss of the protons and hence a wider excitation window, the impact of width fluctuations can be reduced [10,44,45] For more details about the original TSC method and its applications, see Ref. [46].

For the ^{93}Nb$(p, \gamma)^{94}$Mo reaction TSC matrices were constructed which contain all γ-ray events that are part of a two-step cascade, i.e., two γ rays that were detected within a time window of 500 ns. The application of this technique is illustrated in Fig. 5, where the top panel shows the projection of the TSC matrix on the axis of the sum-peak energy. The resulting TSC sum spectrum contains the sum energy of all two-step events. Peaks are visible at energies which represent the population of a discrete state in ^{94}Mo [cf. Eq. (9)]. By

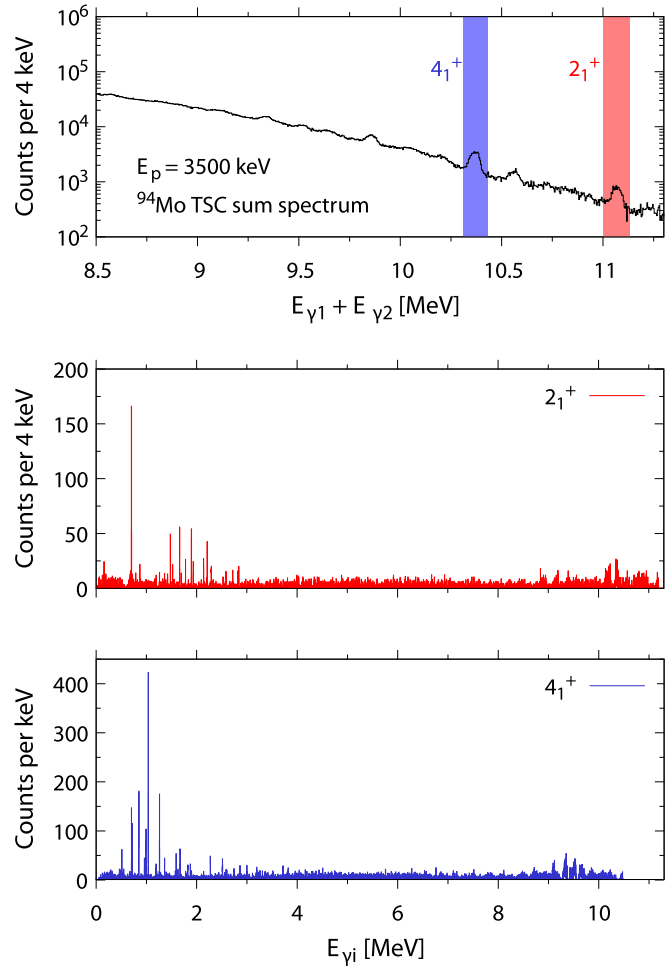

FIG. 5. The projection of the TSC matrix on the axis of summed γ-ray energies for ^{94}Mo (top panel). The TSC spectra for gates on cascade energies populating the 2_1^+ state (middle) and the 4_1^+ state (bottom) are shown as well. By construction, for each low-lying γ-ray in the TSC spectra a high-energetic one was detected as well. However, due to the better energy resolution, the low-lying peaks have higher intensity and much smaller widths.

setting a gate on one of these peaks, all single γ rays become visible which populate the respective state as part of a two-step cascade. Thus, by construction of this matrix, for every primary (high-energetic) γ ray a low energy γ ray can be found. As explained in Sec. III B, the intensity of the primary γ-ray transition can be deduced from the intensity of the low-energy γ-ray. This method has two advantages compared to fitting the high-energetic γ-ray lines in the singles spectra directly: First, the discrete γ-ray lines do not suffer from the energy loss of the protons within the target material, hence they allow a much more precise selection of the final states. Second, due to the much smaller peak widths at lower γ-ray energies, the quality of the peak fitting procedure is improved significantly.

The TSC technique was applied for both proton beam energies of $E_p = 3000$ keV and $E_p = 3500$ keV, allowing us to study the dependence of the γ-ray decay behavior on the excitation energy. In total, primary γ-ray intensities into 34

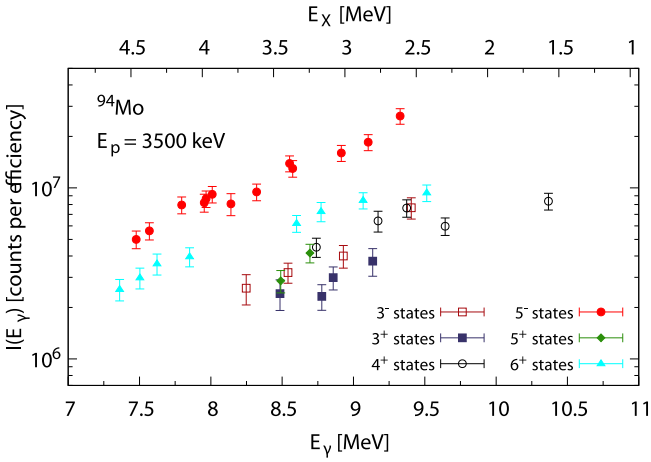

FIG. 6. The measured intensities of primary γ-rays from the discrete TSC spectra. All intensities are corrected for detection efficiencies. Transitions into 5^- and 6^+ states are the most prominent and populated states can be assigned a spin-parity based on the trend of the intensity into states with well-known J^π. In particular, high-energetic 5^- and 6^+ states in ^{94}Mo can be identified with this technique.

($E_p = 3000$ keV) and 40 ($E_p = 3500$ keV) individual excited states in ^{94}Mo were obtained.

As mentioned earlier, the strength of a primary γ-ray depends on the spin and parity of the final state. By means of the particle-γ coincidence technique presented in Sec. IV B one can exclude certain spins and parities based on the γ-ray decay behavior by assuming only $E1$, $M1$, and $E2$ transitions with a sizable intensity. However, according to Eq. (2), for the intensity of primary γ-rays into final levels with the same spin and parity only a dependency on the γ-ray energy and the γ-SF remains. Hence, we expect to find a distinctive trend for these intensities compared to their respective γ-ray energy for each group of J^π. Figure 6 shows the experimental primary γ-ray intensities for the population of states with spins of 3^-, 3^+, 4^+, 5^-, 5^+, and 6^+. Each curve was assigned its respective J^π based on the known level scheme at low excitation energies below $\approx$3 MeV. Especially for the 5^- and 6^+ states a clear trend is observed and for primary γ rays into formerly unknown high energetic states a spin-parity assignment is possible. In the present case, this technique was used to assign a J^π of 5^- to the levels 20 ($E_X = 2835$ keV), 29 ($E_X = 3027$ keV), 46 ($E_X = 3367$ keV), and 51 ($E_X = 3389$ keV). The detection sensitivity limit was found to be at about 2×10^6 events (corrected for efficiency) which corresponds to a cross section of about 0.17 μb.

V. ANALYSIS AND γ-RAY STRENGTH FUNCTION STUDIES

The obtained primary γ-ray intensities were used to explicitly study the γ-ray strength function in ^{94}Mo. Various questions should be addressed within the scope of this analysis: (1) Is it possible to deduce reliable γ-SF values from radiative proton capture experiments? (2) Are there fundamental structures of the dipole strength than can be explored with this technique? (3) Are the obtained values independent from the excitation energy, i.e., can we observe limits of the generalized Brink-Axel hypothesis [48,49]?

This section is structured as follows: In Sec. V A partial cross sections are used to derive γ-ray SF data. The experimental partial cross sections will be compared to theoretical calculations. It will be shown that the deviations between them can be traced back to the γ-ray SF. In a second approach, we use an iterative algorithm to fit explicit $E1$ and $M1$ strength functions which give the best reproduction of the experimental cross sections when used as input for the theoretical calculations. Also, we will use discrete two-step cascade spectra to derive the γ-ray SF in ^{94}Mo in Sec. V B. Finally, a comparison of the derived γ-ray SF data obtained from all three methods is given along with previously published data extracted by means of other techniques in Sec.. V C.

A. Primary γ-ray intensities from partial cross sections

The procedure to extract γ-SF data from the partial cross-section results is very similar to that described in Ref. [32]. Essentially, the experimental partial cross sections are compared to theoretical predictions using the TALYS code [50]. The remaining deviations between TALYS calculations and experimental cross sections are most likely governed by uncertainties in the γ-SF, specifically the $E1$ and $M1$ strengths in ^{94}Mo. In order to actually allocate the deviations to the dipole strength we need to exclude the effect of the nuclear level density (NLD) on the outcome of the predicted partial cross sections. Additionally, we need to disentangle the impact of $E1$ and $M1$ strengths.

The first issue was addressed by constraining the NLD to the cumulative number of low-lying levels. Therefore, we use the microscopic level density from Hilaire's combinatorial tables [51] and properly adjust it according to the description in Refs. [31,32]. In addition to the low-lying levels in ^{94}Mo which are reported in the literature we also included all newly identified levels (see Sec. IV B). We obtained excellent agreement using the same set of parameters as in Ref. [31]. Figure 7 shows the cumulative number of levels in ^{94}Mo plus levels identified in our experiment along with predictions from the microscopic NLD models with the same parametrization as shown in Fig. 7 of Ref. [31].

For the separation of electric and magnetic dipole strengths the respective impact on each calculated partial cross section was investigated. To investigate the contributions of $E1$ and $M1$, each partial cross section was calculated with three different inputs for the dipole strength functions. First, we calculated the cross sections with no modifications on the γ-SF. In a second step, each cross section was calculated without allowing $E1$ or $M1$ transitions, respectively. In order to not tamper with the total γ-ray decay width, $E1$ ($M1$) transitions were only omitted for the respective γ-ray energy of the partial transition. Hence, it was ensured that the general γ-ray decay behavior is not changed, only the population of a certain discrete level via $E1$ or $M1$ transitions is suppressed. Figure 8 shows the contributions of $E1$ and $M1$ transitions to the total intensity of all measured partial cross sections. Apparently, transitions into states with negative

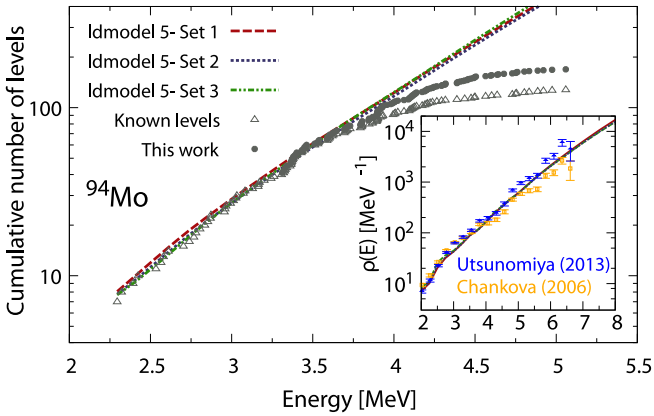

FIG. 7. Cumulative number of levels in ^{94}Mo. Levels known from previous studies [40] are marked as open triangles and new levels that were identified for the first time in this work as closed circles. The predictions of three different parametrizations of the microscopic NLD model from Hilaire *et al.* [51] are in excellent agreement with the low-lying levels. The inset shows the extracted level densities from Oslo-type experiments along with calculated level densities [23,47]. For more information, see Ref. [31].

parity ($\gamma_{11}, \gamma_{14}, \gamma_{20}, \gamma_{29}, \gamma_{46}, \gamma_{51}$) are dominated by $E1$ strength and transitions into states with positive parity ($\gamma_2, \gamma_7, \gamma_{12}, \gamma_{17}$) by $M1$ strength. For the transitions γ_{10} and γ_{23}, which denote the population of 6^+ states, the $M1$ contribution is only slightly larger than that of $E1$.

1. *Ratio of theoretical and experimental partial cross sections*

We started our calculations with the microscopic Gogny D1M plus quasiparticle random-phase approximation (QRPA) model for the $E1$ strength function [52]. For the $M1$ strength we employed the standard Lorentzian. As we show later, our analysis is in general independent from the γ-SF model, however in recent experimental studies these models performed

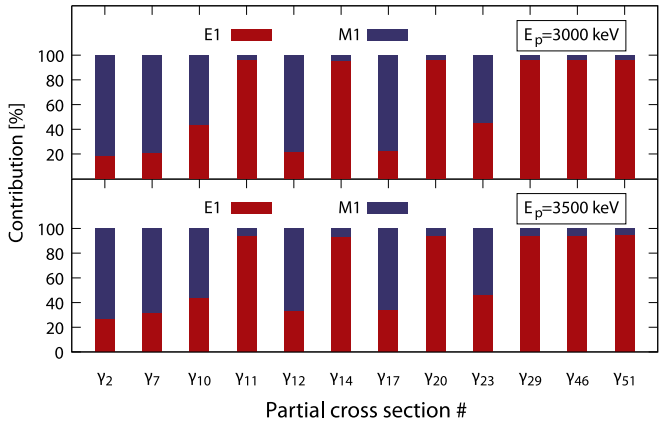

FIG. 8. Contributions from $E1$ and $M1$ transitions to the total intensity of each partial cross section measured in this work. In particular, the prompt population of states with negative parity ($\gamma_{11}, \gamma_{14}, \gamma_{20}, \gamma_{29}, \gamma_{46}, \gamma_{51}$) are almost completely dominated by $E1$ transitions (red) and hence are well suited to study the $E1$ strength function.

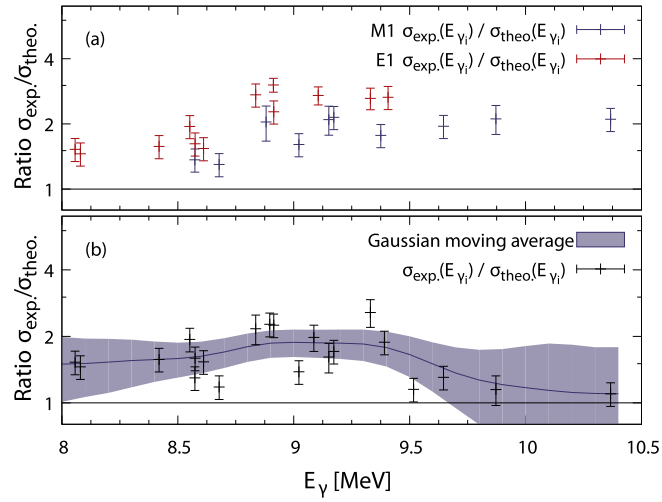

FIG. 9. The upper panel (a) shows the ratio between the experimental partial-cross section values and those from TALYS calculations. Some of the partial cross sections are dominated by the $M1$ strength function and some by the $E1$ strength function. In the lower panel (b) a $M1$ strength function was fitted to properly describe the $M1$-dominated cross sections. The remaining deviations are governed by the $E1$ strength function. A Gaussian moving average algorithm was used to interpolate the data points. It shows qualitatively that an enhancement of the $E1$ strength at around 9.2 MeV is required.

excellently [23,31,32,53]. The ratio between calculated and experimental partial cross-section values was determined separately for transitions that are dominated by $E1$ and $M1$, respectively. Figure 9 shows that partial cross sections which are dominated by $M1$ transitions (blue) are constantly underpredicted by a factor of about 2 for γ-ray energies above 8.7 MeV. On the other hand, partial cross sections that are dominated by $E1$ transitions show larger deviations, in particular at γ-ray energies of around 9.2 MeV. Below $E_\gamma \approx 8.7$ MeV the deviations seem to decrease. No significant dependency on the excitation energy was found, the obtained ratios seem to be only affected by the γ-ray energy.

Subsequently, the $M1$ strength function was scaled to reduce the deviations between experimental and theoretical $M1$-dominated partial cross sections. The remaining deviations can now be traced back solely to the electric dipole strength in ^{94}Mo (see lower panel in Fig. 9). An interpolation function was calculated using a Gaussian moving average algorithm. Possibly, a weak enhancement of the $E1$ strength can be observed at energies of around 9.2 MeV, shortly below the neutron separation threshold of 9.68 MeV. Beyond this qualitative analysis, we want to determine $E1$ and $M1$ strength functions explicitly, next. In Sec. V C we will calculate absolute values for the γ-ray SF by means of the interpolation function.

2. *Calculation of explicit E1 and M1 strength functions by means of a Bayesian optimization algorithm*

In addition to the results presented above, we want to find the explicit shapes of the $E1$ and $M1$ strength functions

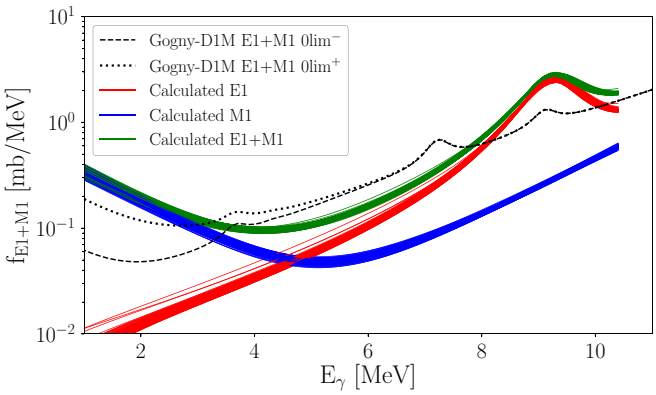

FIG. 10. Calculated $E1$ (red curve) and $M1$ (blue) strength functions in ^{94}Mo that provide the best reproduction of the experimental total and partial cross sections of the ^{93}Nb$(p,\gamma)^{94}$Mo reaction within a 95% confidence interval. All calculated $M1$ strength functions show an enhancement towards lower γ-ray energies whereas the $E1$ strength function clearly shows a resonance at $E_\gamma \approx 9.3$ MeV. The sum of $E1$+$M1$ (green) also features the low-energy up-bend and the resonant behavior as explained before. For details see text.

that minimize the deviations between calculated and experimental partial cross sections. Therefore, we calculated iteratively numerous input strength functions by means of a Bayesian hyperparameter optimization algorithm [54]. Subsequently, for each input strength function partial cross-sections were calculated with TALYS. For both $E1$ and $M1$ strengths, a modified Lorentzian was used, similar to Ref. [44]:

$$f(E_\gamma) = 8.68 \times 10^{-8}\ (\mathrm{mb^{-1}MeV^{-2}}) \times C_{M1}\left[\frac{\sigma E_\gamma \Gamma^2}{\left(E_\gamma^2 - E_R^2\right)^2 + E_\gamma^2\Gamma^2} + Ae^{(-BE_\gamma)}\right] \times e^{C(E_\gamma - E_X)}. \quad (11)$$

Essentially, this Lorentzian allows a low-energy enhancement by an additional exponential function. The $M1$ scaling parameter C_{M1} is included to account for the systematic experimental observation of the f_{M1}/f_{E1} ratio which varies between 0.1 and 0.7. The same Lorentzian has been employed previously, hence we refer to Ref. [31] for more details. In addition, we included a possible enhancement of the dipole strength caused by a pygmy dipole resonance (PDR) for $E1$ and $M1$:

$$f_{\mathrm{PDR}}(E_\gamma) = \frac{\sigma_{\mathrm{PDR}} E_\gamma \Gamma_{\mathrm{PDR}}^2}{\left(E_\gamma - E_{\mathrm{PDR}}^2\right)^2 + E_\gamma \Gamma_{\mathrm{PDR}}^2}, \quad (12)$$

where σ, Γ, and E_{PDR} denote the strength, width, and position of the pygmy dipole resonance. By means of an iterative optimization of the parameters A, B, C, and C_{M1} as well as the strength, position, and width of the PDR, the $E1$ and $M1$ strength functions that give the best reproduction of the experimental partial cross sections were determined. Since the total ^{93}Nb$(p,\gamma)^{94}$Mo cross section is also affected by the dipole strength function, we included the experimental total cross-section values from Ref. [31] in our chi-squared minimization algorithm. Figure 10 shows the calculated $E1$ and $M1$ strength functions that reproduce the experimental total and partial cross sections within a 95% confidence interval. It is noteworthy that all calculated $E1$-SFs exhibit a significant PDR at around 9.3 MeV, which was already suggested based on the results from the preceding subsection. For comparison, we also show the predictions from the D1M+QRPA+0lim model [9]. This is an extension of the D1M+QRPA absorption strength function to the deexcitation strength function. One of its most fundamental features is the low-energy enhancement which was observed in many $M1$ shell model calculations [55–57] or, as mentioned earlier, in several experiments [10–14].

B. Primary γ-ray intensities from TSC spectra

The intensities of primary γ rays into levels with different final spin and parity generate specific curves (as shown in Fig. 6). In order to investigate the dependency on the excitation energy, the primary γ-ray intensities $I(E_\gamma)$ for both particle beam energies of $E_p = 3.0$ MeV and 3.5 MeV were normalized to the respective amount of proton-capture reactions $N(p,\gamma)$:

$$I_{\mathrm{renorm.}} = \frac{I(E_\gamma)}{N_{(p,\gamma)}}. \quad (13)$$

From these intensities relative strength curves were calculated by means of Eq. (10) for each individual spin and parity. Subsequently, since the relative γ-ray strength should only depend on the γ-ray energy, all of these curves were normalized to the curve representing the population of states with $J^\pi = 4^+$. The scaling factors were calculated from the weighted mean of interpolated strength values for the same γ-ray energy. Details of this procedure and a detailed investigation of the uncertainties are given in Ref. [35]. Some of the observed transitions in the discrete TSC spectra belong to the population of the same level. For these, weighted averages were used to obtain the final intensity. For the scaling procedure only curves which contain at least three different states with the given spin and parity were taken into account. Otherwise, no reliable scaling was possible. For the proton beam energy of 3.0 MeV only the values for the population of 4^+, 5^-, and 6^+ states were used.

For each spin-parity curve for which at least three data points are available, Eq. (10) was applied do disentangle the contributions of $E1$ and $M1$ strength. By normalizing the dipole strength onto the highest-energetic transition, a set of linear equations is obtained and can be solved unambiguously. Since in the studied energy range the $E1$ strength dominates the $M1$ strength by at least one order of magnitude, it was found that Eq. (10) can be approximated by

$$\frac{I_{L_1}}{I_{L_2}} \approx \frac{f_{E1}(E_{\gamma_1})}{f_{E1}(E_{\gamma_2})} \times \frac{E_{\gamma_1}^3}{E_{\gamma_2}^3}, \quad (14)$$

and the ratio method yields information about the $E1$ strength function. However, since the $M1$ strength function is much smaller, it turned out that very different $M1$ values deliver the same ratios. Consequently, using this ratio technique only the $E1$ strength was extracted.

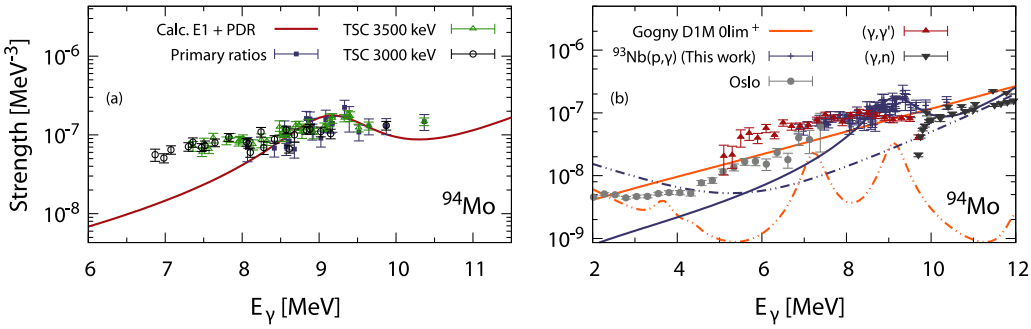

FIG. 11. (a) Absolute γ-SF values extracted in this work by means of partial cross sections (blue squares) and the discrete TSC spectra from the ^{93}Nb$(p,\gamma)^{94}$Mo reaction. For the latter one the ratio method (see. Sec. V B) was employed and the obtained values are separately shown for both proton beam energies of $E_p = 3000$ keV (black circles) and 3500 keV (green triangles). In addition we show the best results of the explicit calculation of $E1$ strength functions. The calculated $E1$ strength function as well as our distinct data points exhibit a $E1$ resonance at $E_\gamma \approx 9.3$ MeV. (b) Comparison of the results with previously published experimental results using the Oslo technique [14,23], (γ,γ') measurements [25], and photoabsorption experiments [23,24]. In addition, predictions from the Gogny D1M+QRPA γ-SF model [52] using the recent zero-limit adjustment [9] are shown. For our explicit strength-function calculations as well as for the theoretical Gogny model we show the $E1$ strength as a dashed line and the $M1$ strength as a dashed-dotted line.

The final γ-SF curves for both beam energies are plotted in Fig. 11 and exhibit a smooth trend. Hence, we assume that there is no violation of the generalized Brink-Axel hypothesis when comparing the results at 11.46 and 11.96 MeV excitation energy in ^{94}Mo.

C. The dipole strength function in ^{94}Mo

Finally, we want to compare the γ-SF data which were extracted by the different methods presented in this paper to other experimental data and existing theoretical models. Above the neutron separation energy of $S_n = 9.68$ MeV photoabsorption data from (γ,n) experiments are available [23,24] and below S_n photon-scattering data from a (γ,γ') experiment [25]. The γ-SF data extracted from Oslo-type experiments extend the measured energy region to very low γ-ray energies [14,23]. In Fig. 11 the results from these experiments are shown along with the γ-SF data deduced in this work. From the explicit calculations using the Bayesian algorithm we chose the $E1$ and $M1$ strength functions which give the best reproduction of the partial cross sections ($\chi^2_{\text{red}} = 1.71$).

The significant up-bend at low γ-ray energies is in good agreement with results from the Oslo experiment as well as with the theoretical predictions from the D1M+QRPA+0lim model [9] and can be explained by the $M1$ strength function in ^{94}Mo. However, compared to the D1M+QRPA calculations our extracted $M1$ strength is higher than predicted and does not yield the predicted resonances. Since the aforementioned $M1$ model is not able to reproduce the experimental cross sections, we conclude that a deeper investigation of the theoretical modeling is necessary.

A different picture arises for the $E1$ strength function. Our calculated $E1$ strength function is in good agreement with the D1M+QRPA model above γ-ray energies of $\approx$8 MeV. Although the resonance which was observed in our experiment at a γ-ray energy of around 9.3 MeV is not reproduced, the D1M+QRPA $E1$ model is well suited to reproduce the experimental cross sections of the ^{93}Nb$(p,\gamma)^{94}$Mo reaction. The overall adjustment that was applied to describe the partial cross sections (see Sec. V A 1) is below a factor of 2.

We also calculated absolute γ-SF values using the obtained ratios between experimental and partial cross sections. Therefore, we employed the Gaussian interpolation function which is shown in part (b) of Fig. 9 and scaled the D1M+QRPA $E1$ strength function accordingly. This way, absolute strength values are obtained which are in good agreement with the results from the TSC technique and are well described by the calculated $E1$ strength function.

Only two of our experimental γ-SF values are above the neutron separation threshold of $S_n = 9.68$ MeV, hence no meaningful comparison to existing photoneutron experiments can be drawn. Our calculated strength functions are in good agreement with the results from (γ,n) experiments [23,24]. Below S_n we extracted γ-SF values down to γ-ray energies of about 7 MeV. The absolute values are in very good agreement with (γ,γ') data which were derived from bremsstrahlung experiments [25]. However, significant discrepancies below $E_\gamma \approx 7$ MeV remain between the (γ,γ') data and the results from Oslo-type experiments.

D. Systematics of the γ-ray strength function in even-even Mo isotopes

To test the validity of the Brink-Axel hypothesis it has to be ensured that experimentally obtained γ-ray strength functions are free from systematic uncertainties that are governed by the specific method which was used to derive them. Consequently, extracted strength functions should be independent from the employed experimental method. Recently, large experimental campaigns were carried out aiming at studying the γ-ray strength function in stable Mo isotopes. In particular, on nearly all even-even $^{92-100}$Mo isotopes strength function data over a wide range of γ-ray energies are available which were obtained from (γ,n) [23,24,58], (γ,γ') [25], or Oslo-type

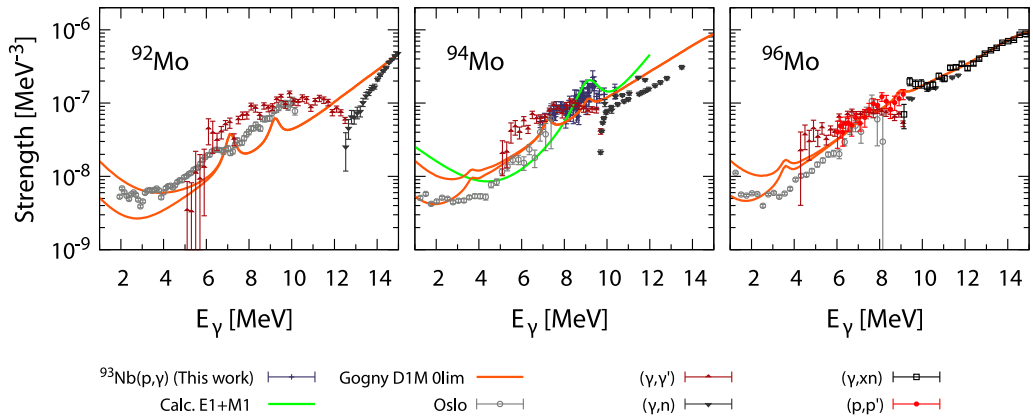

FIG. 12. Comparison between the extracted sum of electric and magnetic dipole strength functions derived from photoneutron experiments [23,24,58], particle-γ coincidence measurements employing the Oslo method [14,23,59], and (γ, γ') experiments [25] for $^{92-96}$Mo. Results derived from (p, p') measurements are available for ^{96}Mo [60]. Predictions from the Gogny D1M+QRPA+0lim [9] model are also included for the summed $E1$ and $M1$ strengths. For ^{94}Mo, our data obtained from the ^{93}Nb$(p, \gamma)^{94}$Mo experiment are included and demonstrate that proton-capture experiments represent a complementary technique to deduce γ-ray strength functions.

experiments [14,23,59]. As already shown in Ref. [23], the shape and absolute values of the γ-SF below the neutron threshold differ significantly for the different methods. In Fig. 12, we expand the current picture for the even-even isotopes $^{92-96}$Mo, where all existing experimental data are shown. For ^{94}Mo the results from this work are included and for ^{96}Mo recent results from a ^{96}Mo(p, p') experiment have been added [60].

VI. SUMMARY AND CONCLUSION

In this paper we reported on the primary γ-ray intensities from the ^{93}Nb$(p, \gamma)^{94}$Mo reaction at two different beam energies and how these results can be used to study the γ-ray strength in ^{94}Mo. We presented two different methods of how the primary γ-ray intensities can be obtained. First, the direct analysis of the γ-ray peaks in the singles spectra was possible and via the comparison of the respective *partial cross section* to statistical model calculations conclusions about the γ-SF can be drawn. A second attempt is the construction of two-step-cascade spectra. From those spectra, the intensity of first generation γ-rays can be deduced from the intensity of their respective *second generation* γ rays and their absolute branching ratios. Employing the ratio technique allows one to calculate relative strength functions for transitions into final states with the same spin and parity. After a normalization, a smooth trend for the extracted strength function was found which showed no violation of the generalized Brink-Axel hypothesis in this case. In addition, explicit $E1$ and $M1$ strength functions were calculated by means of a Bayesian hyper parameter optimization algorithm to minimize the deviations between experimental total and partial cross sections and cross sections obtained from statistical model calculations.

In summary, from the radiative proton-capture on ^{93}Nb absolute γ-SF values could be extracted in ^{94}Mo. An increase of the $E1$ strength function just below S_n is observed. The observable energy range of primary γ rays is restricted by the Q value of the reaction, and this allowed the study of the dipole strength down to a γ-ray energy of about 7 MeV in the present case. In order to go to even lower γ-ray energies and possibly solve the deviations between data from (γ, γ') and Oslo-type experiments, a lower proton-beam energy is required.

We showed that radiative proton-capture reactions are a well-suited tool to investigate the statistical γ-decay behavior in atomic nuclei and allow to investigate the γ-ray strength function over a wide range of γ-ray energies below and above the neutron separation threshold. In addition, this technique allows the study of the γ-ray strength function in unstable nuclei that can be reached via proton capture.

ACKNOWLEDGMENTS

We are grateful to K. O. Zell and A. Blazhev for the target preparation and H. W. Becker, V. Foteinou, and D. Rogalla of the Ruhr-Universität Bochum for the assistance during the RBS measurements. This project was supported by the Deutsche Forschungsgemeinschaft under the contracts ZI 510/8-2.

APPENDIX: LOW-ENERGY DECAY BEHAVIOR OF ^{94}Mo

Table II lists all low-lying levels in ^{94}Mo which show at least two γ decays to lower lying levels as well as all newly identified levels.

TABLE II. Low-energy decay behavior of ^{94}Mo. All levels with more than one measured normalized γ-decay intensity I_γ are shown as well as newly identified levels. The γ-ray energy E_γ is calculated from the initial level energy E_X and the final level energy E_f. Values for E_X, E_f, and J^π are taken from Ref. [40]. The uncertainties of I_γ are statistical only, except where noted separately. Upper limits for I_γ are given to compare with $I_{\gamma,Lit.}$ values and are preceded by "$\lesssim$". For all γ-ray energies and level energies an uncertainty of ± 1 keV is assumed. Parts of the results were already published in Ref. [41].

E_X (keV)	J_i^π	E_f (keV)	J_f^π	E_γ (keV)	I_γ (%)	$I_{\gamma,\mathrm{Lit.}}$ (%)
1864	2^+	871	2^+	993	100.0(6)	100.0(8)
		0	0^+	1864	10.2(2)	8.9(11)
2067	2^+	871	2^+	1196	100.0(8)	100.0(7)
		0	0^+	2067	14.0(4)	15.1(7)
2295	4^+	1574	4^+	721	100.0(11)	100.0(2)
		871	2^+	1424	11.6(7)	13.3(2)
2393	2^+	871	2^+	1522	100.0(11)	100(2)
		0	0^+	2393	12.5(6)	11.1(2)
2534	3^-	2067	2^+	467	52.7(3)	57.3(10)
		1864	2^+	670	35.1(2)	31.9(13)
		1574	4^+	960	67.9(3)	81(3)
		871	2^+	1663	100.0(3)	100(2)
2565	4^+	1574	4^+	991	100(13)	100.0(8)
		871	2^+	1694	12(2)	11.8(8)
2740	1^+	2067	2^+	673	$\lesssim 8$	3.0(5)
		1864	2^+	876	$\lesssim 13$	24.4(5)
		1742	0^+	998	$\lesssim 6$	4.4(1)
		871	2^+	1869	100(3)	100(2)
		0	0^+	2740	71(4)	65.4(13)
2768	4^+	1574	4^+	1194	59.6(11)	71(4)
		871	2^+	1897	100.0(12)	100(4)
2805	3^+	1864	2^+	941	64(4)	63(4)
		1574	4^+	1231	90(5)	100(5)
		871	2^+	1934	100(4)	76(3)
2835	$(5)^-$[a]	2611	$(5)^-$	224	14(2)	7.2(10)
		2565	4^+	270	10(2)	
		2534	3^-	301	15(5)[b]	13.1(12)
		1574	4^+	1261	100(3)	100
2870	2^+	2393	2^+	477	12.5(11)	
		2067	2^+	803	10.6(12)	26(2)
		1864	2^+	1006	100(2)	100(4)
		871	2^+	1999	11.3(10)	13.1(6)
		0	0^+	2870	19.3(14)	17.3(5)
2965	3^+	2565	4^+	400	9(2)	
		2067	2^+	898	21(2)	23.0(12)
		1864	2^+	1101	100(3)	100(2)
		1574	4^+	1392	65(3)	63(2)
		871	2^+	2094	42(3)	36.9(14)
2993	2^+	2393	2^+	600	47(3)	
		2067	2^+	926	43(2)	45(3)
		1864	2^+	1129	99(4)	100(4)
3012	3^-	2534	3^-	478	60.7(11)	51(2)
		2393	2^+	618	2.0(4)	
		2067	2^+	944	12.7(5)	12(2)
		1864	2^+	1147	19.1(6)	12(2)
		1574	4^+	1438	17.8(7)	37(3)
		871	2^+	2140	100.0(13)	100(2)
3027	(5^-)[a]	2611	$(5)^-$	416	100(2)	100(4)
		2534	3^-	493	80(2)	60(4)
3072	$(2, 3^+)$	2703	(3^-)	369	11.4(13)	
		2534	3^-	539	17(2)	12(2)
		1864	2^+	1208	100(2)	100(5)
		871	2^+	2201	46(4)	37(2)
3082	$(3)^+$[a]	2703	(3^-)	379	7.2(13)	
		2295	4^+	788	18(2)	
		1864	2^+	1218	$\lesssim 7$	14(2)
		1574	4^+	1509	46(3)	
		871	2^+	2211	100(5)	100(2)
3129	1^+	2067	2^+	1061	$\lesssim 7$	1.2(1)
		1864	2^+	1264	23(2)	18.3(4)
		871	2^+	2258	3.8(12)	4.3(1)
		0	0^+	3129	100(4)	100.0(3)
3163	$(3)^+$[a]	2870	2^+	293	5.5(4)	
		2805	3^+	358	7.4(5)	16.7(13)
		2067	2^+	1096	1.1(7)	
		1864	2^+	1299	9.5(9)	
		871	2^+	2292	100(2)	100.0(13)
3261	1^-	2067	2^+	1194	9(2)[c]	
		1742	0^+	1519	19.2(8)	
		871	2^+	2390	12.3(7)	67[?]
		0	0^+	3261	100(2)	100(17)
3311[*]		871	2^+	2440	100	
3366	(5^-)[a]	2965	3^+	401	16.0(13)	24(4)
		2534	3^-	832	43(2)	
		2295	4^+	1071	100(2)	100(4)
3368	(6^-)[a]	2611	$(5)^-$	757		100
		2423	6^+	945		50(3)
3398	(3^-)[a]	1574	4^+	1824	100	
3429	(2,3)[d]	3072	$(2, 3^+)$	357	52(11)[b]	
		2805	3^+	624	29(6)[b]	
		2740	1^+	689	46(30)[b]	
		2067	2^+	1362	50(5)	
		1864	2^+	1565	60(5)	
		871	2^+	2558	100(5)	100
3456	(3^+)[a]	3027	(5^-)	429	1.7(4)	
		3012	3^-	444	7.6(4)	
		2965	3^+	491	3.2(9)	
		2870	2^+	586	4.8(4)	
		2565	4^+	891	4.1(5)	

TABLE II. (*Continued.*)

E_X (keV)	J_i^π	E_f (keV)	J_f^π	E_γ (keV)	I_γ (%)	$I_{\gamma,\mathrm{Lit.}}$ (%)
		2534	3^-	922	31.9(9)	
		2067	2^+	1389	52.2(12)	
		1864	2^+	1592	11.7(5)	
		1574	4^+	1882	17.2(9)	
		871	2^+	2585	100(2)	
3512	$1^{(+)}$	2740	1^+	772	33(16)[b]	
		1742	0^+	1770	40(20)[b]	49(9)
		871	2^+	2641	44(22)[b]	51.6(13)
		0	0^+	3512	100(6)	100.0(11)
3589	(4^-)[a]	2611	$(5)^-$	978	100	
3592*		2295	4^+	1297	6.8(13)	
		1574	4^+	2018	25(2)	
		871	2^+	2721	100(4)	
3620	(5^-)[a]	3027	(5^-)	593	36(5)	
		2611	5^-	1009	100(6)	
3640*	(2^+)[d]	2067	2^+	1573	53(3)	
		1864	2^+	1776	84(3)	
		1742	0^+	1898	35(2)	
		1574	4^+	2066	31(2)	
		871	2^+	2769	89(4)	85(7)[e]
		0	0^+	3640	100(3)	100(8)[e]
3693	(3^-)[a]	2835	(5^-)	858	13.2(11)	
		2768	4^+	925	36(2)	100(22)[f]
		1864	2^+	1829	15.1(14)	
		871	2^+	2822	100(2)	95(22)
3714		2534	3^-	1181	53(6)	
		871	2^+	2843	100(9)	
3792	2^+	2393	2^+	1399	48(2)	55(3)
		2067	2^+	1725	8.0(14)	
		1864	2^+	1928	100(2)	100(4)
		1574	4^+	2217	24.2(12)	
		871	2^+	2921	8.5(12)	
		0	0^+	3792	80(3)	78(2)
3800	(5^-)[a]	2611	5^-	1190	100	
3843*		1574	4^+	2269	100(4)	
		871	2^+	2972	27(3)	
3847	(4)[a]	3027	(5^-)	820	100(3)	
		2565	4^+	1281	64(3)	
		2295	4^+	1552	33(3)	100
		1864	2^+	1983	43(8)	
		1574	4^+	2274	77(5)	
3889*		871	2^+	3018	100(3)	
		0	0^+	3889	24(3)	
3897	$3^+, 5^+$[g]	2768	4^+	1130	69(5)	
		2295	4^+	1604	100(5)	100
		1864	2^+	2033	16(3)	
3900	(2^+)[g]	2067	2^+	1832	29(4)	
		1574	4^+	2326	100(4)	
		871	2^+	3029	82(6)	
3910*		2423	6^+	1487	100	
3914*		2565	4^+	1349	45(4)	

TABLE II. (*Continued.*)

E_X (keV)	J_i^π	E_f (keV)	J_f^π	E_γ (keV)	I_γ (%)	$I_{\gamma,\mathrm{Lit.}}$ (%)
		2295	4^+	1619	35(4)	
		1574	4^+	2340	100(4)	
3926*		0	0^+	3926	100	
3930*	(5^-)[a]	2835	$(5)^-$	1095	100	
3936*		2295	4^+	1641	100(7)	
		871	2^+	3065	62(5)	
3957*		871	2^+	3086	100	
3973*	(5^-)[a]	2835	$(5)^-$	1138	100	
3979*		871	2^+	3108	100	
3987*	(5^-)[a]	2611	5^-	1376	100(9)	
		2564	3^-	1423	72(9)	
		2295	4^+	1692	24(5)	
3990*		2535	3^-	1455	14.7(14)	
		1864	2^+	2126	23(2)	
		1574	4^+	2415	23(2)	
		871	2^+	3118	100(3)	
		0	0^+	3990	8.4(12)	
4089*	(6^+)[a]	2611	5^-	1478	47(2)	
		2295	4^+	1795	20(2)	
		2067	2^+	2022	16.8(12)	
		1865	2^+	2224	23(2)	
		1574	4^+	2515	100(2)	
		871	2^+	3218	85(3)	
4102*		1574	4^+	2528	100(5)	
		871	2^+	3231	83(6)	
4113	(3^-)	2293	2^+	1820	100(4)	
		2067	2^+	2046	41(5)	
4127	(3^-)[g]	2067	2^+	2060	82(5)	
		871	2^+	3256	22(8)	
4136*		3072	$(2, 3^+)$	1064	38(3)	
		871	2^+	3264	100(3)	
		0	0^+	4136	65(4)	
4145*	(5^-)[a]	2835	(5^-)	1310	24(12)	
		2611	5^-	1536	100(50)	
4191	(2^+)	3082	$(3)^+$	1109	96(11)	
		871	2^+	3321	100(8)	
		0	0^+	4191	79(10)	
4205*		871	2^+	3334	33(3)	
		0	0^+	4205	100(5)	
4242*		871	2^+	3371	100	
4251*		3368	(6^-)	883	100	
4298*		871	2^+	3427	100	
4313*	(6^+)[a]	1574	4^+	2739	100(5)	
		871	2^+	3442	48(8)	
4318	2^+[g]	3012	3^-	1306	100	
4372*	(5^-)[a]	2611	$(5)^-$	1761	100	
4390*		0	0^+	4390	100(2)	
4395*		2535	3^-	1860	100(3)	
		1574	4^+	2821	19(3)	
4409*		871	2^+	3538	100	
4424*		2067	2^+	2357	94(10)	
		1864	2^+	2559	55(11)	

TABLE II. (*Continued.*)

E_X (keV)	J_i^π	E_f (keV)	J_f^π	E_γ (keV)	I_γ (%)	$I_{\gamma,\mathrm{Lit.}}$ (%)
		871	2^+	3553	100(9)	
		0	0^+	4424	35(10)	
4436	(6^+)[a]	1574	4^+	2862	100	
4451*		1864	2^+	2586	87(10)	
		871	2^+	3580	100(8)	
4454*		3082	$(3)^+$	1372	100(4)	
		3072	$(2, 3^+)$	1382	71(7)	
		0	0^+	4454	46(9)	
4462*	(5^-)[a]	2835	(5^-)	1627	100	
4490*		871	2^+	3619	100	
4505*		2067	2^+	2437	100(4)	
		871	2^+	3633	45(4)	
		0	0^+	4505	21(5)	
4577*	(6^+)[a]	1574	4^+	3003	100	
4595*		871	2^+	3724	100(5)	
		0	0^+	4595	54(5)	
4644*		0	0^+	4644	100	
4678*		0	0^+	4678	100	
4761*		0	0^+	4761	100	

[a]From the primary γ-ray intensity into this level a (new) spin-parity assignment was performed.
[b]The determination of the peak volume was difficult, so the uncertainty of the area determination was incorporated in the uncertainty stated here.
[c]In the decay cascade of this level, a γ ray of similar energy is emitted. As the relative uncertainties are known, this contribution was eliminated.
[d]From the γ-decay behavior of this level, a tentative spin and/or parity assignment can be derived.
[e]Taken from Ref. [61].
[f]A γ-ray of the same energy is also emitted from the 2993 keV state and its contributions might not be taken into account here.
[g]A level very close to the derived excitation energy here is reported in Ref. [40]. The reported J^π is given here.
*The excitation energy of this level was calculated from the γ-ray energies reported here for the first time.
?Marked as uncertain (?) in Ref. [40].

[1] E. M. Burbidge, G. R. Burbidge, W. A. Fowler, and F. Hoyle, Rev. Mod. Phys. **29**, 547 (1957).
[2] M. Arnould, S. Goriely, and K. Takahashi, Phys. Rep. **450**, 97 (2007).
[3] F. Käppeler, R. Gallino, S. Bisterzo, and W. Aoki, Rev. Mod. Phys. **83**, 157 (2011).
[4] M. Pignatari, R. Gallino, M. Heil, M. Wiescher, F. Käppeler, F. Herwig, and S. Bisterzo, Astrophys. J. **710**, 1557 (2010).
[5] M. Arnould and S. Goriely, Phys. Rep. **384**, 1 (2003).
[6] T. Rauscher, N. Dauphas, I. Dillmann, C. Fröhlich, Zs. Fülöp, and Gy. Gyürky, Rep. Prog. Phys. **76**, 066201 (2013).
[7] M. Pignatari, K. Göbel, R. Reifarth, and C. Travaglio, Int. J. Mod. Phys. E **25**, 04 (2016).
[8] R. Capote *et al.*, Nucl. Data Sheets **110**, 3107 (2009).
[9] S. Goriely, S. Hilaire, S. Péru, and K. Sieja, Phys. Rev. C **98**, 014327 (2018).
[10] A. Voinov, E. Algin, U. Agvaanluvsan, T. Belgya, R. Chankova, M. Guttormsen, G. E. Mitchell, J. Rekstad, A. Schiller, and S. Siem, Phys. Rev. Lett. **93**, 142504 (2004).
[11] A. C. Larsen *et al.*, J. Phys. G: Nucl. Part. Phys. **44**, 064005 (2017).
[12] A. C. Larsen *et al.*, Phys. Rev. Lett. **111**, 242504 (2013).
[13] E. Litvinova and N. Belov, Phys. Rev. C **88**, 031302(R) (2013).
[14] M. Guttormsen *et al.*, Phys. Rev. C **71**, 044307 (2005).
[15] D. Savran, T. Aumann, and A. Zilges, Prog. Part. Nucl. Phys. **70**, 210 (2013).
[16] A. C. Larsen and S. Goriely, Phys. Rev. C **82**, 014318 (2010).
[17] S. Goriely, Phys. Lett. B **436**, 10 (1998).
[18] S. Goriely *et al.*, Eur. Phys. J. A **55**, 172 (2019).
[19] M. Rayet, M. Arnould, M. Hashimoto, N. Prantzos, and K. Nomoto, Astron. Astrophys. **298**, 517 (1995).
[20] S. E. Woosley and W. M. Howard, Astrophys. J. Suppl. **36**, 285 (1978).
[21] S. Jin, L. F. Roberts, S. M. Austin, and H. Schatz, Nature (London) **588**, 57 (2020).
[22] W. Rapp, J. Görres, M. Wiescher, H. Schatz, and F. Käppeler, Astrophys. J. **653**, 474 (2006).
[23] H. Utsunomiya *et al.*, Phys. Rev. C **88**, 015805 (2013).
[24] A. Banu, E. G. Meekins, J. A. Silano, H. J. Karwowski, and S. Goriely, Phys. Rev. C **99**, 025802 (2019).
[25] G. Rusev, R. Schwengner, R. Beyer, M. Erhard, E. Grosse, A. R. Junghans, K. Kosev, C. Nair, K. D. Schilling, A. Wagner, F. Dönau, and S. Frauendorf, Phys. Rev. C **79**, 061302 (2009)(R).
[26] J. Isaak *et al.*, Phys. Lett. B **788**, 225 (2019).
[27] M. Wiedeking *et al.*, Phys. Rev. Lett. **108**, 162503 (2012).
[28] F. Heim, J. Mayer, M. Müller, P. Scholz, M. Weinert, and A. Zilges, Nucl. Instrum. Methods A **966**, 163854 (2020).
[29] J. Ziegler, J. Biersack, and M. Ziegler, SRIM - The Stopping and Range of Ions in Matter, http://srim.org/
[30] G. A. Bartholomew, E. D. Earle, A. J. Ferguson, J. W. Knowles, and M. A. Lone, Adv. Nucl. Phys. **7**, 229 (1973).
[31] F. Heim, P. Scholz, J. Mayer, M. Müller, and A. Zilges, Phys. Rev. C **101**, 035807 (2020).
[32] F. Heim, P. Scholz, M. Körschgen, J. Mayer, M. Müller, and A. Zilges, Phys. Rev. C **101**, 035805 (2020).
[33] S. Harissopulos, A. Spyrou, V. Foteinou, M. Axiotis, G. Provatas, and P. Demetriou, Phys. Rev. C **93**, 025804 (2016).
[34] L. Netterdon, A. Endres, S. Goriely, J. Mayer, P. Scholz, M. Spieker, and A. Zilges, Phys. Lett. B **744**, 358 (2015).

[35] P. Scholz, M. Guttormsen, F. Heim, A. C. Larsen, J. Mayer, D. Savran, M. Spieker, G. M. Tveten, A. V. Voinov, J. Wilhelmy, F. Zeiser, and A. Zilges, Phys. Rev. C **101**, 045806 (2020).
[36] H. Junde, H. Su, and Y. Dong, Nucl. Data Sheets **112**, 1513 (2011).
[37] E. Browne and J. K. Tuli, Nucl. Data Sheets **111**, 1093 (2010).
[38] J. Mayer, G4Horus - Geant4 simulation for Horus, 2019, https://gitlab.ikp.unikoeln.de/jmayer/g4horus.git
[39] N. Agostinelli, *et al.*, Nucl. Instrum. Methods A **506**, 250 (2003).
[40] D. Abriola and A. A. Sonzogni, Nucl. Data Sheets **107**, 2423 (2006).
[41] S. G. Pickstone *et al.*, Nucl. Instrum. Methods A **875**, 104 (2017).
[42] A. Hoogenboom, Nucl. Instrum. Methods **3**, 57 (1958).
[43] F. Bečvář, P. Cejnar, R. E. Chrien, and J. Kopecký, Phys. Rev. C **46**, 1276 (1992).
[44] A. Voinov, S. M. Grimes, C. R. Brune, M. Guttormsen, A. C. Larsen, T. N. Massey, A. Schiller, and S. Siem, Phys. Rev. C **81**, 024319 (2010).
[45] A. Voinov *et al.*, EPJ Web Conf. **93**, 01022 (2015).
[46] F. Bečvář *et al.*, Nucl. Instrum. Methods B **261**, 930 (2007).
[47] R. Chankova *et al.*, Phys. Rev. C **73**, 034311 (2006).
[48] D. M. Brink, Ph.D. thesis, Oxford University, 1955 (unpublished).
[49] P. Axel, Phys. Rev. **126**, 671 (1962).
[50] A. Koning and D. Rochman, Nucl. Data Sheets **113**, 2841 (2012).
[51] S. Hilaire and S. Goriely, Nucl. Phys. A **779**, 63 (2006).
[52] M. Martini, S. Péru, S. Hilaire, S. Goriely, and F. Lechaftois, Phys. Rev. C **94**, 014304 (2016).
[53] V. Foteinou *et al.*, Eur. Phys. J. A **55**, 67 (2019).
[54] J. Bergstra, D. Yamins, and D. D. Cox, in *Proceedings of the 30th International Conference on Machine Learning (ICML 2013)*, edited by S. Dasgupta and D. McAllester (ACM, New York, 2013), pp I-115–I-123.
[55] R. Schwengner, S. Frauendorf, and A. C. Larsen, Phys. Rev. Lett. **111**, 232504 (2013).
[56] B. A. Brown and A. C. Larsen, Phys. Rev. Lett. **113**, 252502 (2014).
[57] R. Schwengner, S. Frauendorf, and B. A. Brown, Phys. Rev. Lett. **118**, 092502 (2017).
[58] H. Beil, R. Bergere, P. Carlos, A. Lepetre, A. De Miniac, and A. Veyssiere, Nucl. Phys. A **227**, 427 (1974).
[59] G. M. Tveten *et al.*, Phys. Rev. C **94**, 025804 (2016).
[60] D. Martin *et al.*, Phys. Rev. Lett. **119**, 182503 (2017).
[61] V. Derya *et al.*, Nucl. Phys. A **906**, 94 (2013).